

We are IntechOpen, the world's leading publisher of Open Access books Built by scientists, for scientists

6,900

Open access books available

186,000

International authors and editors

200M

Downloads

Our authors are among the

154

Countries delivered to

TOP 1%

most cited scientists

12.2%

Contributors from top 500 universities



WEB OF SCIENCE™

Selection of our books indexed in the Book Citation Index
in Web of Science™ Core Collection (BKCI)

Interested in publishing with us?
Contact book.department@intechopen.com

Numbers displayed above are based on latest data collected.
For more information visit www.intechopen.com



Structural and Electron Transport Properties of Ultrathin SiO₂ Films with Embedded Metal Nanoclusters Grown on Si

Andrei Zenkevich¹, Yuri Lebedinskii¹, Oleg Gorshkov²,
Dmitri Filatov² and Dmitri Antonov²

¹National Research Nuclear University "Moscow Engineering Physics Institute"

²N.I. Lobachevskii University of Nizhnii Novgorod
Russia

1. Introduction

During the last decade, much attention has been focused on the investigation of the semiconductor and metal nanocrystals (NCs) embedded in the dielectric matrices. The interest was generated by the promising applications of the nanocomposite structures in nanoelectronics. Particularly, the semiconductor or metal NCs embedded in the dielectric layer of a metal-insulator-semiconductor field-effect transistor (MOSFET) may replace the SiN_x floating gates in the nonvolatile memory devices, allowing for thinner injection oxides, and subsequently, smaller operating voltages, longer retention times, and faster write/erase speeds (Tiwari et al., 1996). The performance of such memory devices strongly depends on the parameters of NCs arrays, such as their size, shape, spatial distribution, electronic band alignment, as well as on the possibility to make reproducibly the uniform tunnel transparent oxide films.

The charge accumulation in the NCs can be limited by the single-electron effects such as Coulomb blockade provided that the cluster has a sufficiently small size, which, in principle, allows for the single electron memory devices (Yano et al., 1994; Guo et al., 1997).

Up to the present time, the thin film nanocomposite structures have been studied extensively (Ruffino et al., 2007). The most popular methods to fabricate NCs in the dielectric matrices include low-energy ion implantation with subsequent annealing (Bonafos et al., 2000), the deposition of the non-stoichiometric oxide layers also followed by the annealing (Tiwari et al., 2000), and the deposition of the multilayered oxide/NC structures (Ruffino & Grimaldi, 2007).

The main disadvantage of the ion implantation is a considerable thickness of the layer where the NCs are nucleating, and also a rather large dispersion in the NCs' sizes. The latter fact is a direct consequence of the NCs' nucleation by Ostwald ripening. The largest NCs with the minimum density are concentrated at the mean projected ion path, while the smaller NCs with higher density are nucleated in the tails of the implanted ions depth distribution. Recent attempts to improve the ion implantation technique to address the above problems are concerned mainly about the reduction of the ion energy down to ~ 1

keV or less (Ren et al., 2009). However, it requires a considerable complication of the implanters to provide a high enough ion beam density at low ion energies.

The SiO₂ layers containing the Si or Ge NCs arranged in single sheet(s) can be obtained by deposition of the thin (3 to 7 nm) suboxidized SiO_x (GeO_x, $x = 1.3$ to 1.7) layers sandwiched between the SiO₂ spacers, e. g., by electron beam or magnetron sputtering followed by annealing (Zacharias et al, 2002). However, the NC size dispersion inside the layers due to their nucleation through Ostwald ripening still remains an unresolved problem. More recently, ordered multilayered arrays of the Au NCs have been fabricated using the self-assembling effects in nucleation of the Au NCs on the surface of SiO₂ spacer layer both deposited by magnetron sputtering (Cho et al., 2004).

In this chapter, the two novel approaches to the fabrication of the ultrathin SiO₂/SiO₂:NC-Me/SiO₂/Si (Me = Au, Pt) nanocomposite structures are described. One of these approaches is based on the room temperature deposition of an ultrathin mixed Si – Me amorphous film by Pulsed Laser Deposition (PLD) combined with the further oxidation of the Si-Me mixture in the glow discharge oxygen plasma in a single vacuum cycle (Zenkevich et al., 2009). Another one exploits the effect of metal segregation during the thermal oxidation of the pre-deposited ultrathin Si–Me layers. Both approaches allowed the fabrication of the single sheet two-dimensional arrays of the Me NCs sandwiched between the two ultrathin SiO₂ layers with precisely controlled thickness.

Among the other ones, the SiO₂:NC-Au material system is of a special interest. Silicon is known to have an extremely high diffusivity in Au, that promotes the phase segregation in the SiO₂– Au system even at low temperatures (Hiraki et al., 1972). Since Au and Si do not form any stable chemical compound and there is no stable gold oxide, Au can be expected to precipitate into the NCs during the oxidation of the Au–Si mixture. In this scope, it is important to have an initial uniform amorphous mixture of Au and Si atoms. PLD technique, owing to its pulsed nature and low deposition rates (0.01–0.05 monolayers (ML) per pulse) allows a precise control over both the composition and the thickness of the depositing layer, and hence is particularly suitable technique to prepare uniform mixed layers by sequential deposition from the elemental targets.

The structural properties of thus fabricated nanocomposite structures as well as the metrology of the metal NCs, including their spatial and size distribution in the dielectric matrix as a function of the initial Me/Si ratio as well as of the processing conditions will be described. The structural properties of the ultrathin SiO₂/SiO₂:NC-Me/SiO₂/Si layers will be further related to their electronic properties. The electron tunnelling through the individual metal NCs embedded in the ultrathin dielectric films have been investigated using Tunnelling Atomic Force Microscopy (AFM) technique. The Au NCs sandwiched between the ultrathin SiO₂ layers on the conductive Si substrates are visualized in the Tunnelling AFM images of the nanocomposite films as the spots of increased probe current (or the current channels) and attributed to the electron tunnelling through the individual Au NCs. The tunnelling spectra of the nanocomposite films measured in the current channels exhibit a Coulomb staircase at room temperature, while a negative differential resistance is observed in the spectra measured in the smallest current channels ascribed to the resonant electron tunnelling through the size-quantized Au NCs. Finally, a theory describing the imaging of the metal NCs embedded into a thin dielectric film on a conductive substrate is presented.

2. Growth and characterization of the SiO₂:nc-metal nanocomposite films

The investigated SiO₂/SiO₂:NC-Me/SiO₂ nanocomposite structures have been grown in an ultrahigh vacuum (UHV) setup based on Kratos® XSAM-800 electron spectrometer. The schematic of the growth setup is presented in Fig. 1. This setup allows the growth of the multilayered nanocomposite structures by PLD (including reactive PLD in various gas ambient) combined with the thermal/plasma oxidation and the analysis of the deposited layers *in situ* by the combination of surface sensitive techniques, particularly, by X-ray Photoemission Spectroscopy (XPS).

The deposition of the SiO₂:NC-Me films was carried out in the preparation chamber of the Kratos® XSAM-800 spectrometer, equipped with PLD module based on the pulsed YAG:Nd Q-switched laser. The second harmonic of the YAG:Nd laser radiation was used (the emission wavelength $\lambda \approx 532$ nm). The energy in the laser pulse was varied in the range from 0.1 to 0.3 J, the pulse duration was ≈ 15 ns, and the repetition rate was set 25 Hz.

The SiO₂/SiO₂:NC-Au/SiO₂ films for the Tunnelling AFM investigations were grown on the As doped *n*⁺-Si(001) substrates with the resistivity of $\rho \approx 0.002$ Ohm·cm. The Si substrates were chemically cleaned to remove native oxide prior to loading into the preparation chamber using a standard Radio Corporation of America (RCA) treatment. It is worth noting that XPS revealed no traces of the oxide on the Si substrate surface after loading in UHV.

The process of SiO₂/SiO₂:NC-Au/SiO₂/Si nanocomposite structures growth using the glow discharge oxygen plasma oxidation is shown schematically in Fig. 2. All the steps of the growth process were performed at room temperature. First, a the uniform SiO₂ layers with the thickness $d_u \sim 1$ nm were formed by the glow discharge plasma oxidation of the chemically cleaned Si substrates (Fig. 2, *a*). The partial pressure of oxygen p_O in the preparation chamber during the oxidation was $p_O \sim 10^{-2}$ mbar, the discharge voltage U was maintained in the range from 500 to 800 V.

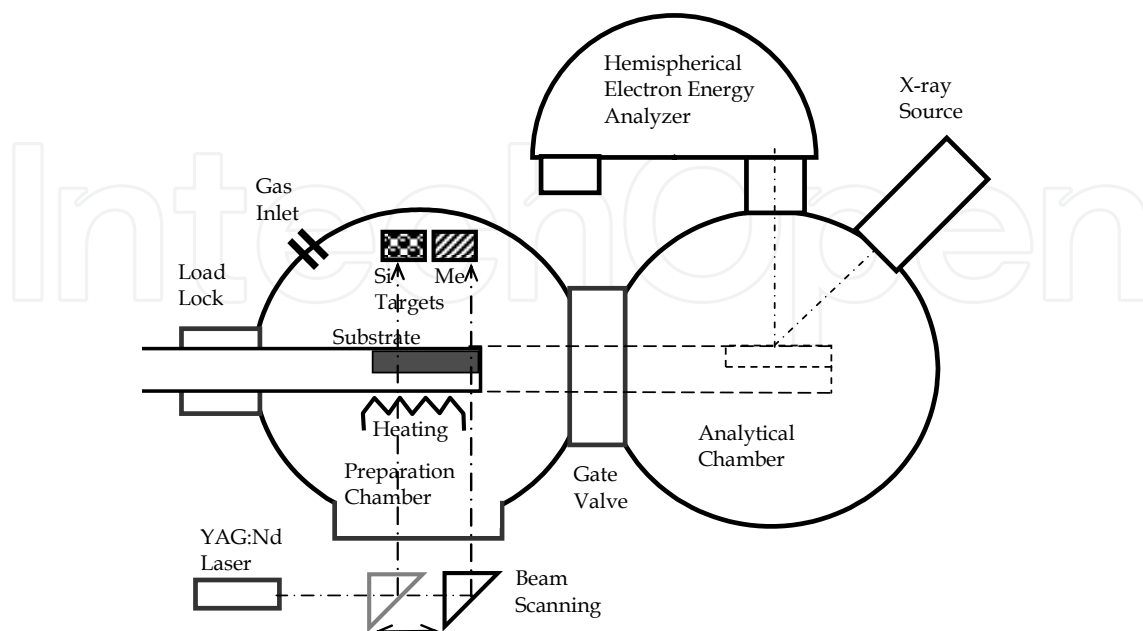


Fig. 1. The schematic of the growth setup.

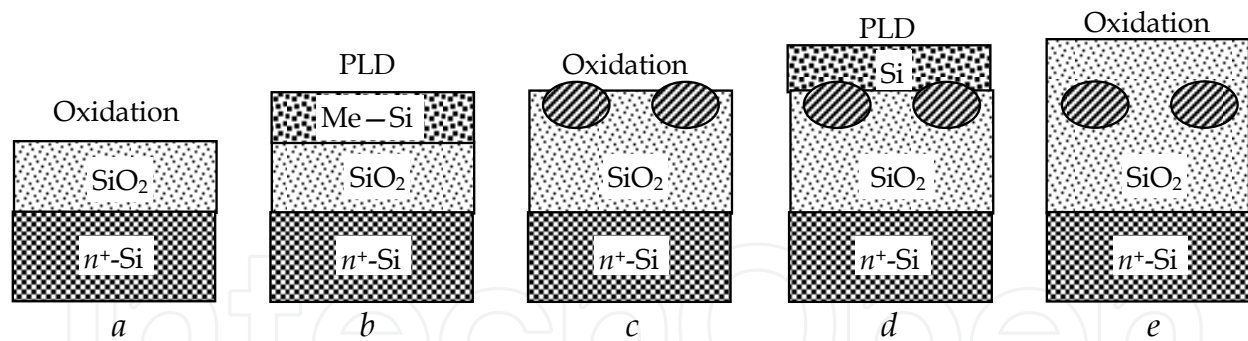


Fig. 2. The schematic of the $\text{SiO}_2/\text{SiO}_2:\text{NC-Me}/\text{SiO}_2/n^+\text{-Si}$ structure growth using the combination of PLD and the oxidation in the glow discharge plasma.

The ultrathin mixed amorphous Au–Si layers with the thickness $d_{\text{Au-Si}} \sim 1$ nm (Fig. 2, b) were deposited onto the SiO_2 surface by sequential deposition of the submonolayer portions of Au and Si from the elemental targets mounted inside the preparation chamber (Fig. 1). The Au/Si composition ratio was varied from 0.15 to 0.5 by varying the number of pulses per each target. The laser beam was alternately directed onto Si and Au targets. A computerized double prism beam scanning system was used both for raster scanning of the laser beam over the targets' surface and for switching from one elemental target to another according to the deposition program. The calibration of the Au and Si deposition rates was made by Rutherford Backscattering Spectrometry (RBS) using He^+ ions with the energy of 1.5 to 2 MeV. RUMP® software was used to analyze the RBS spectra. According to RBS, the deposition rate was $\sim 10^{13}$ atoms/cm² (~ 0.1 ML) per a pulse and depended on the specific target.

At the next step, the Au–Si mixture layer was oxidized in the glow discharge oxygen plasma at the same parameters as were used in growing the underlying SiO_2 layer. The oxidation has resulted in the precipitation of the Au NCs in and/or at the surface of the SiO_2 layer (Fig. 2, c). Finally, to cap the formed Au NCs, a ~ 1 nm thick amorphous Si layer was deposited on top and oxidized in the oxygen plasma (Fig. 2, d and e).

The process of the $\text{SiO}_2/\text{SiO}_2:\text{NC-Au}/\text{SiO}_2$ nanocomposite structure growth was monitored *in situ* by XPS in the analytical chamber of Kratos® XSAM-800 spectrometer (Fig. 1) as described in detail elsewhere (Lebedinskii et al., 2005). The XPS analysis provided the information on the chemical state of the film constituents as well as on the layers' thickness at each step of the growth process. The latter was calculated using the well-known procedure based on the attenuation of the respective XPS lines by the growing layers (Hochella Jr. & Carim, 1988). In particular, the thickness of the underlying SiO_2 layer (Fig. 2, a) was calculated as

$$d_u = \lambda_a \ln \frac{I_0}{I_1}, \quad (1)$$

where I_0 and I_1 are the intensities of the Si 2p XPS line recorded from the bare Si substrate and upon its oxidation, respectively (Fig. 3, spectrum 1), and $\lambda_a \approx 2.4$ nm is the free path of the photoelectrons with the energy $E \approx 100$ eV in SiO_2 . For the room temperature glow discharge plasma oxidation of Si surface d_u was found to vary depending on the oxidation time, but was limited to ≈ 3 nm.

The evolution of the XPS Si 2*p* and Au 4*f* lines during SiO₂/SiO₂:NC-Au/SiO₂/*n*⁺-Si structure growth is presented in Fig. 3. Upon deposition of the mixed Si–Au layer (Fig. 2, *b*), an additional component of the Si 2*p* line appears in the XPS spectrum (Fig. 3, spectrum 2). In addition, a shift of the Au 4*f* line with respect to the metallic Au reference spectrum (cf. spectra 2 and 6 in Fig 3) is observed. Both effects indicate the formation of a metastable Au silicide. The thickness of the deposited Si–Au layer was set to be less than 2 nm to ensure its full oxidation in the glow discharge oxygen plasma at the next step (Fig. 2, *c*). Upon oxidation (Fig. 3, spectrum 3), the Au 4*f* line is shifted close to its position in bulk metallic Au, while the silicide component of the Si 2*p* line is converted into the Si⁴⁺ indicating the formation of SiO₂. From these changes the formation of the Au precipitates in or at the surface of the SiO₂ layer is evident.

Upon deposition of the amorphous Si onto the SiO₂:NC-Au layer (Fig. 2, *d*), the formation of the Au silicide bonds is again clearly observed in XPS spectra (Fig. 3, cf. spectra 4 and 2). This observation we take as an evidence that at least some of the precipitated Au NCs are not embedded in the SiO₂ layer.

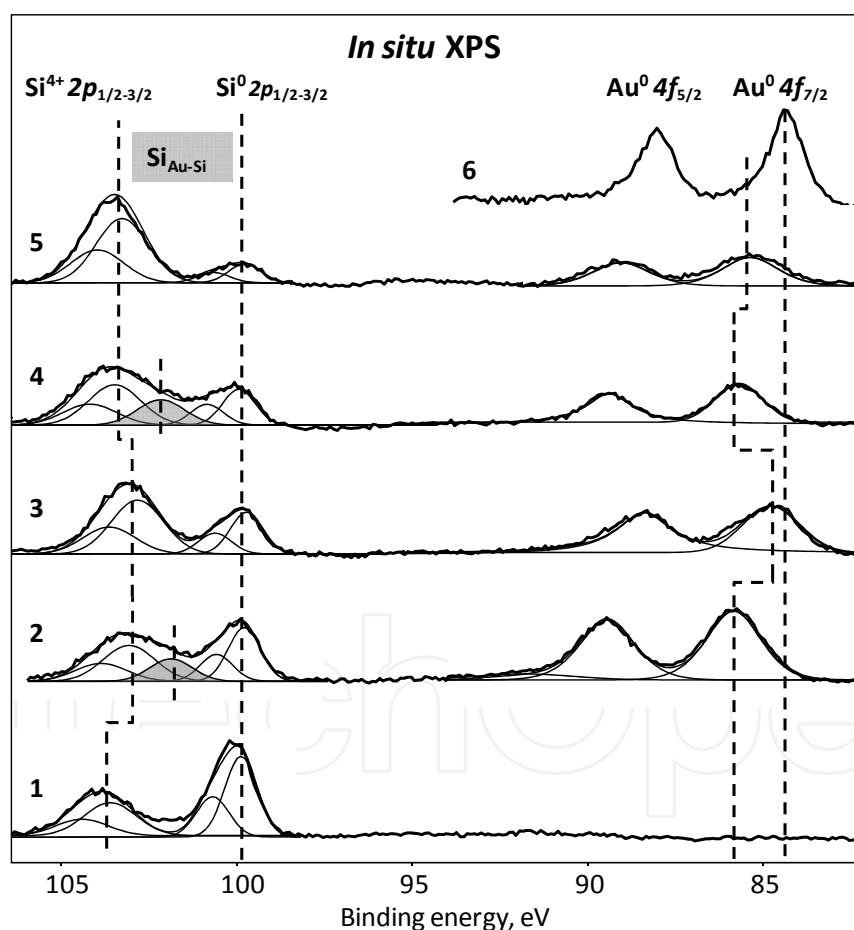


Fig. 3. The evolution of the XPS spectra during the growth of a SiO₂/SiO₂:NC-Au/SiO₂/*n*⁺-Si(001) nanocomposite structure. 1 – upon oxidation of the Si substrate in the glow discharge oxygen plasma; 2 – upon deposition of the mixed Au–Si layer; 3 – upon oxidation of the Au–Si layer; 4 – after deposition of the amorphous Si cap layer; 5 – after oxidation of the latter; 6 – the spectrum of the bulk metallic Au (reference). Reprinted from (Zenkevich et al., 2009), with permission from ©Elsevier®.

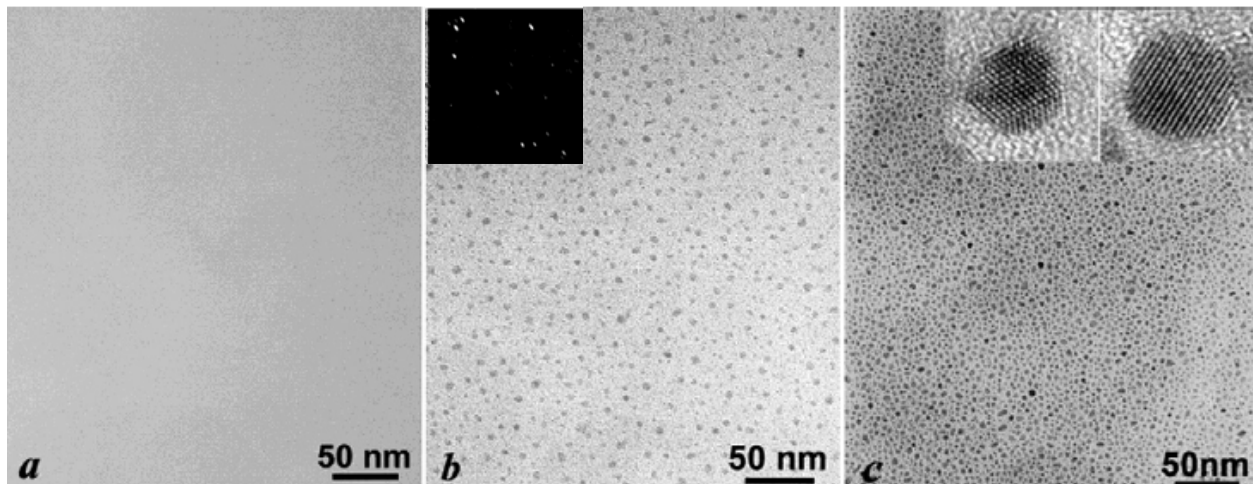


Fig. 4. The plain-view TEM bright-field images of the nanocomposite structures grown on NaCl(100): *a* – Si/Si-Au/Si (reference); *b*, *c* – SiO₂/SiO₂:NC-Au/SiO₂. Au/Si ratio: *a*, *b* – 0.15; *c* – 0.5. Insets: to Fig. *b* – dark-field image indicating the presence of crystalline NCs; to Fig. *c* – the high-resolution TEM images of the individual Au NCs. Reprinted from (Zenkevich et al., 2009), with permission from ©Elsevier®.

Finally, upon the oxidation of the capping amorphous Si layer, the Au 4*f* line is back at metallic Au position again, while all the deposited Si is in the oxidized state (SiO₂). The latter conclusion is evident from the increase of the Si⁴⁺ peak at the expense of the Si⁰ components in the Si 2*p* line (Fig. 3, spectrum 5). The quantitative analysis of the XPS spectra presented in Fig. 3 gives the Au/Si ratio to be ≈ 0.2 , the thickness of the bottom SiO₂, SiO₂:NC-Au and capping SiO₂ layers to be $d_b \approx 1.6$ nm, $d_{NC} \approx 1.6$ nm, and $d_c \approx 1.8$ nm, respectively.

The structural characterization of the nanocomposite structures was carried out with the plain-view Transmission Electron Microscopy (TEM) in the bright- and dark-field geometries using JEOL® JEM 2000EX instrument operating at the beam energy of 180 keV. The nanocomposite SiO₂/SiO₂:NC-Au/SiO₂ structures for the TEM investigations were grown on the freshly cleaved NaCl(001) substrates. Both underlying and cap SiO₂ layers were formed by oxidation of the deposited amorphous Si. In addition, a 10 nm thick amorphous carbon (graphite) film was deposited *in situ* by PLD onto the cap SiO₂ layer to ensure the integrity of the nanocomposite film after the lift-off.

To prove that the precipitation of Au NCs occurs during the oxidation of the mixed Au–Si layer, a reference sample has been grown missing the oxidation steps. Fig. 4, *a* presents a plain-view TEM image of the reference sample. No NCs are observed. In contrast, in the bright-field TEM image of an oxidized sample (Fig. 4, *b*) the Au NCs are clearly visible. The sheet density of the Au NCs N_s is clearly dependent on the Au/Si ratio (cf. Au/Si ratio 0.15 vs. 0.5 in Fig. 4, *b* and *c*, respectively). The dark-field TEM image presented on the inset in Fig. 4, *b* reveals the crystalline structure of the Au NCs as is further evident from the high-resolution TEM images of the individual Au NCs shown on the inset in Fig. 4, *c*. The detailed high resolution TEM analysis reveals both faceted and round shapes of the Au NCs, which is suggested to depend on whether the NCs precipitate near the surface or inside the SiO₂ layer during the oxidation of the Au–Si mixture, respectively. According to the detailed analysis of the plain-view TEM images, the typical values of the lateral size D and the areal density N_s of the Au NCs are 2 to 5 nm and $(1–3) \times 10^{13}$ cm⁻², respectively, subject

to the Au/Si ratio. In order to characterize the spatial distribution of the Au NCs in the nanocomposite structures with different Au/Si ratios, the separations between the nearest neighbors for each NC were calculated from the plain-view TEM images. The distribution of the separations between the NCs ℓ found experimentally were then fitted with the model function derived from the Poisson distribution (valid for a small surface coverage):

$$f(\ell) = 2\pi \exp\left[-\pi N_s (\ell - R_0)^2\right] N_s (\ell - R_0), \quad (2)$$

for $\ell \geq R_0$. Here $R_0 = \langle D \rangle / 2$ is the mean lateral radius of the NCs and the areal density N_s were the fitting parameters. The values of $\langle D \rangle$ and N_s obtained by the fitting of the distributions of ℓ for the samples with different Au/Si ratios were in good agreement with those directly measured from the TEM images. Having determined R_0 and N_s , one can calculate the relative dispersion of the NCs' separation:

$$\frac{\Delta \ell}{\langle \ell \rangle} = \frac{\sqrt{4 - \pi}}{\sqrt{\pi} (2R_0 \sqrt{N_s} + 1)}. \quad (3)$$

It was found that $\Delta \ell / \langle \ell \rangle$ decreased from ≈ 0.28 down to ≈ 0.15 with increasing Au/Si ratio from ≈ 0.2 to ≈ 0.5 .

The kinetics of Au segregation during the plasma oxidation of the ultrathin amorphous Au–Si mixture layers at room temperature has been also analyzed. It should be noted that the oxygen plasma treatment of ultrathin Si and/or Au–Si layers, besides providing the active oxygen atoms, may also produce thermal and radiation effects in the deposited layer worth evaluated. To assess possible heating of the Si substrate surface by the glow discharge plasma with the discharge current $I = 10$ mA at $U = 500$ V during the treatment time $t = 60$ s, one can first estimate the heating expansion length x in Si at given conditions $x \sim (\kappa t / \rho c)^{1/2} \sim 10$ cm (here κ is the thermal conductivity, c is the heat capacity, and ρ is the density of Si) that is much larger than the substrate thickness (≈ 0.3 mm). Thus, the heating of the Si substrate during the plasma treatment is rather uniform in depth, and can be evaluated suggesting the fraction of the total plasma energy $Q = UI t \sim 300$ J incident onto the Si sample surface with the area of ~ 1 cm² while the total chamber area is $\sim 2 \times 10^3$ cm². So far, the heating by the plasma $\Delta T = Q / mc$ (where m is the mass of the Si substrate) appears to be limited to ~ 10 K, and can thus be neglected. The radiation effects of the oxygen glow discharge plasma can certainly play an essential role in the oxidation of the Au–Si ultrathin layers as well as on the kinetics of the Au NCs' precipitation. We suggested that the oxidation starts from the upper Si atoms forming a few ML thick SiO₂. At this stage, the Au–Si chemical bonds are breaking, and due to the local strain and/or radiation heating, the Au atoms receive a sufficient energy to travel a distance of few lattice constants. Due to low solubility of Au in SiO₂, the Au atoms segregate at SiO₂ surface and further nucleate in the NCs. An alternative way is the segregation of Au NCs at the bottom interface of the SiO₂ layer through a well known mechanism of Au segregation by the Si oxidation front due to anomalously high diffusivity of the unoxidized Si atoms through the nucleated Au NCs (Hiraki et al., 1972).

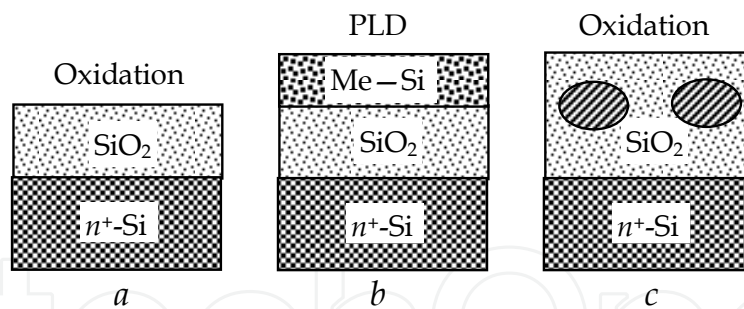


Fig. 5. The schematic of a $\text{SiO}_2/\text{SiO}_2:\text{NC-Me}/\text{SiO}_2/n\text{-Si}$ structure growth using thermal oxidation.

As a result, the two types of the Au NCs precipitating at the surface of the oxidizing Au–Si layer and at the bottom interface with the underlying SiO_2 layer can be expected. The observation by TEM of two types of Au NCs corroborates this suggestion.

In Fig. 5, the schematic of the alternative growth process of the $\text{SiO}_2/\text{SiO}_2:\text{NC-Me}/\text{SiO}_2/n\text{-Si}$ nanocomposite structures using the thermal oxidation of the mixed Me–Si layer is presented. The process consists of the three stages. At the first stage (Fig. 5, a), a SiO_2 layer 6 to 8 nm in thickness is formed by the thermal oxidation of the Si substrate.

The $n\text{-Si}(001)$ substrates doped by phosphorus with the resistivity of $\rho \approx 4.5 \text{ Ohm}\cdot\text{cm}$ have been used. The thermal oxidation of the Si substrates as well as that of the mixed Me–Si layers have been carried out using an industrial SDO-125/4A furnace. The temperature of the oxidation of the Me–Si layers T_A was chosen in the range $T_A = 640 \div 725^\circ\text{C}$, the oxidation time t_A was varied from 1 to 9 hours. At the next stage, the mixed Me–Si layer (Me = Au, Pt) was deposited onto the underlying SiO_2 layer surface by the co-deposition of the noble metal and Si by PLD at the parameters described above.

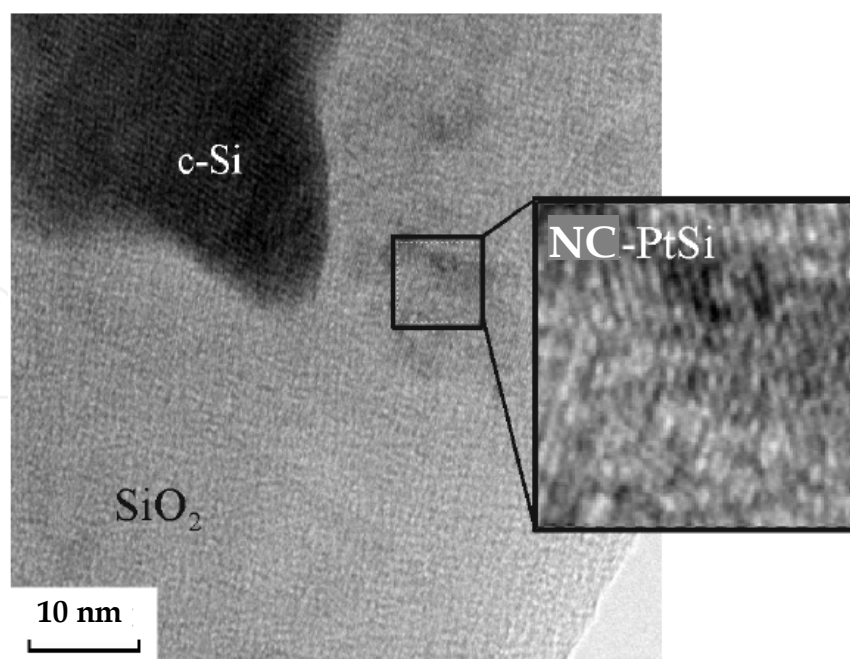


Fig. 6. A plain-view TEM image of the $\text{SiO}_2/\text{SiO}_2:\text{NC-Pt}/\text{SiO}_2/n\text{-Si}$ nanocomposite structure. Reprinted from (Maksimova et al., 2009), with permission from ©Intercontact Science® Publishing.

The Me/Si ratio in the deposited Me–Si layers was varied from 1 : 20 to 1 : 30, the layer thickness was 5 to 20 nm, and the corresponding nominal thickness of the deposited Me layer was 0.5 to 0.7 nm. Finally, the thermal oxidation of the deposited Me–Si layer was performed. During the oxidation process, Me atoms effectively segregate towards the lower interface between the mixed Me–Si layer and the underlying SiO₂ one. The metal NCs segregation process is facilitated by the preferential oxidation of Si, by a low solubility of the noble metals in SiO₂, and by the anomalously high diffusivity of Si through the nucleated metallic NCs. The bottom SiO₂ layer serves as a blocking layer for the segregation process, thus strictly defining the arrangement of the Me NCs in a single sheet.

The TEM investigations of the samples prepared by the thermal oxidation have been carried out using fEI® Tecnai™ G2 30 instrument at the accelerating voltage of 300 kV. A plain view TEM image of the SiO₂/SiO₂:NC-Pt/SiO₂/*n*-Si nanocomposite structure is presented in Fig. 6 *a*. The TEM analysis reveals that besides the Me NCs in the amorphous SiO₂ layer the nano-inclusions of the non-oxidized crystalline Si of ~ 50 nm in size are also present. These inclusions are likely formed at the interface between the Me–Si and the underlying SiO₂ layers. Also the analysis of the micro diffraction patterns shows that during the thermal oxidation of the Pt–Si mixture the platinum silicide NCs (particularly, the phase Pt₂Si) are formed with the size of 5 to 10 nm.

To perform *C*–*V* measurements, the Al contacts with the area of 5×10^{-5} to 8×10^{-4} cm² have been deposited onto the SiO₂ cap layers by PLD through a shadow mask. The back ohmic contacts to the Si substrate were made using In–Ga alloy. In Fig. 7 the *C*–*V* curves of the Al/SiO₂/SiO₂:NC-Me/SiO₂/*n*-Si nanocomposite metal-oxide-semiconductor (MOS) structures grown in various conditions are presented. The high frequency *C*–*V* measurements had been carried out using Keithley® 590 setup at 1 MHz. The *C*–*V* curve measured from the SiO₂/SiO₂:NC-Au/SiO₂/*n*-Si sample produced at the oxidation parameters $T_A = 640^\circ\text{C}$, $t_A = 540$ min (Fig. 7, *a*, curve 1) exhibits a broad hysteresis loop compared to the sample oxidized during $t_A = 300$ min (Fig. 7 *b*, curve 2) where the hysteresis loop is much narrower.

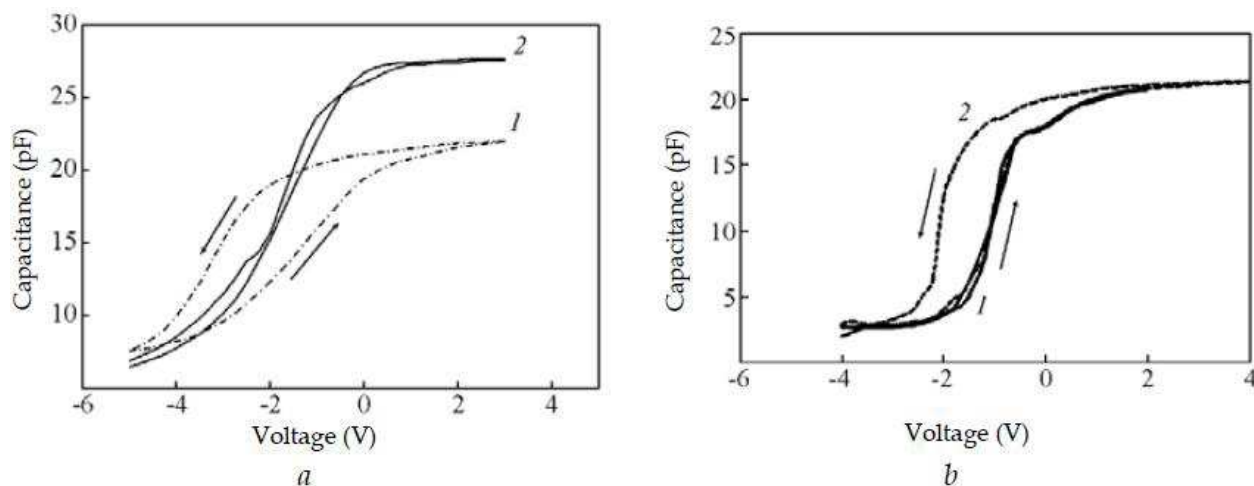


Fig. 7. The *C*–*V* curves of the SiO₂/SiO₂:NC-Me/SiO₂/*n*-Si nanocomposite structures. Me: *a*– Au; *b*– Pt. $T_A = 640^\circ\text{C}$; t_A , min: 1 – 540; 2 – 300. Reprinted from (Maksimova et al., 2009), with permission from ©Intercontact Science® Publishing.

The hysteresis in *C*–*V* curves is ascribed to the charge accumulation in the Me NCs. The smaller value of the saturated capacitance for longer t_A is probably related to the larger total

oxide thickness. It is important to note that almost no hysteresis is observed when the amplitude of the voltage sweep V is less than 2 V, however, a broad hysteresis loop appears when V is increased up to 4 V (Fig. 7, *b*). The dependence of the hysteresis in the $C-V$ curves on the sweep voltage amplitude points at the tunneling mechanism of the filling and the depletion of the NCs with electrons. The electron tunneling rate is determined by the thickness of the bottom SiO_2 layer d_u . Alternatively, the NC-Si grains observed in this sample by TEM (see Fig. 6) can also accumulate the electrons and therefore contribute to the memory effect.

3. Imaging of the metal nanoclusters embedded into the ultrathin dielectric films by Tunnelling AFM

The Tunneling AFM investigations of the $\text{SiO}_2/\text{SiO}_2\text{:NC-Au}/\text{SiO}_2/n^+\text{-Si}$ nanocomposite structures were carried out in Omicron® MultiProbe S™ UHV system at room temperature. The measurement scheme is presented in Fig. 8. The sample surface was scanned across by a Pt coated AFM probe in the contact mode. Simultaneously, the $I-V$ curves of the probe-to-sample contact were acquired in each point of the scan.

Earlier, Tunnelling AFM had been applied mainly to study the defects in the thin dielectric films (Yanev et al., 2008). Antonov et al., 2004 have applied Tunnelling AFM to the investigation of the electron transport through the Zr NCs produced by ion implantation in the $\text{Zr(Y)O}_2/p^+\text{-Si}$ films. Scanning Tunnelling Microscopy (STM) had been used earlier to study the electron transport through the metal NCs dispersed inside the dielectric films (Bar-Sadeh et al., 1994; Imamura et al., 2000). However, the applicability of STM to such objects is limited to the case when the NCs' concentration is high enough, i.e. when the films possess a sufficient percolation conductivity. In this case, keeping the STM feedback is provided by the continuous switching of the tunnelling electrons path through the film (hereinafter referred to as the current channel) from one chain of the NCs to another. The application of the Tunneling AFM allowed the studying of the locally nonconductive $\text{Zr(Y)O}_2\text{:nc-Zr}/p^+\text{-Si}$ films since the feedback (AFM) channel (F_n) and the measuring one (the probe current I_t) were decoupled (Fig. 8).

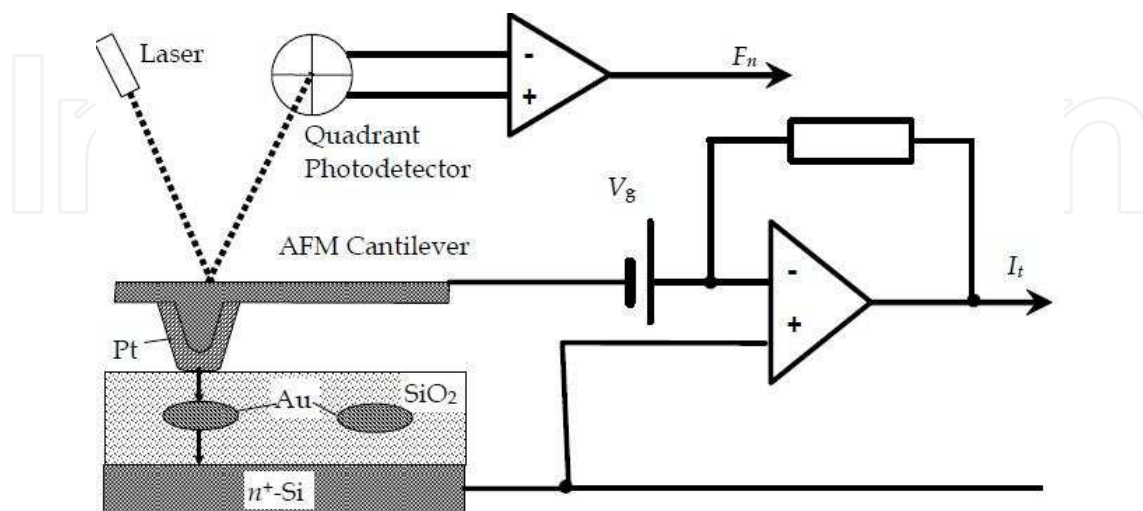


Fig. 8. The schematic of the Tunneling AFM experiment to investigate the electronic properties of a $\text{SiO}_2/\text{SiO}_2\text{:NC-Au}/\text{SiO}_2/n^+\text{-Si}(001)$ nanocomposite structure.

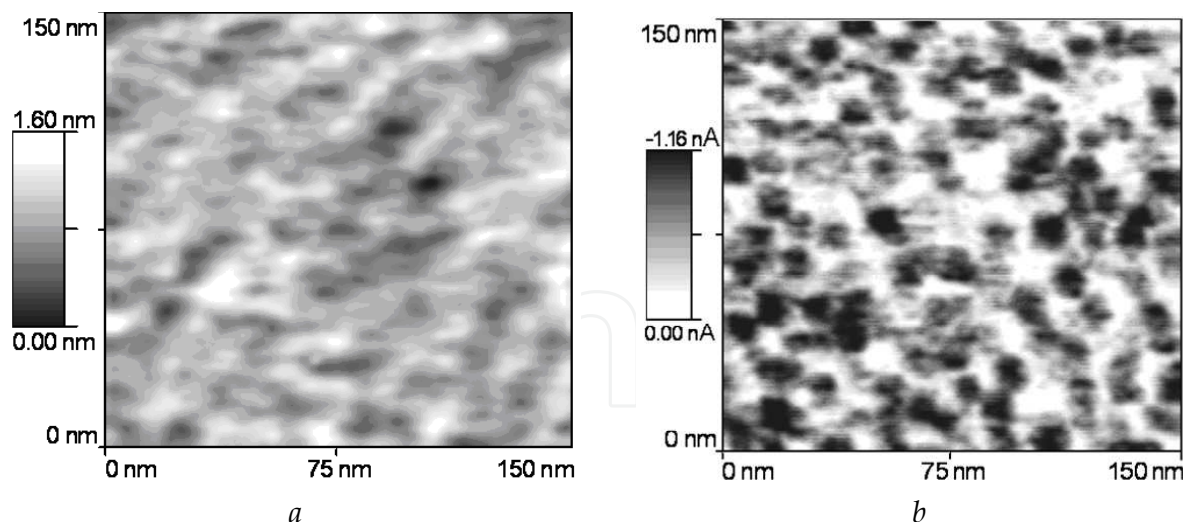


Fig. 9. The AFM (*a*) and the current (*b*) images of the SiO₂(1.5 nm)/ SiO₂:NC-Au/SiO₂(1.5 nm)/*n*⁺-Si(001) nanocomposite structure. $V_g = -2.5$ V. Reprinted from (Filatov et al., 2010) under license by IoP Publishing Ltd.

In Fig. 9 the AFM and current images of the PLD/glow discharge oxidation grown SiO₂(1.5 nm)/SiO₂:NC-Au/SiO₂(1.5 nm)/*n*⁺-Si film are presented. The inverted contrast in the current image in Fig. 9, *b* (the larger the probe current I_t , the darker the area) is related to the negative polarity of the bias voltage applied between the AFM probe and the sample V_g which, in turn, corresponds to the injection of the electrons from the Pt coated AFM tip into the *n*⁺-Si substrate through the nanocomposite film.

The spots of increased I_t or the current channels of 3 to 10 nm in size observed in the current image (Fig. 9, *b*) are attributed to the electron tunnelling through the individual Au NCs. It is worth noting that the current image in Fig. 9, *b* weakly correlates with the AFM one presented in Fig. 9, *a* (the Pearson's correlation coefficient R_P calculated for this particular pair of images was ≈ 0.15).

In order to establish the relationship between the geometrical and electronic properties of the NCs in the current images of the SiO₂/SiO₂:NC-Me/SiO₂/*n*⁺-Si nanocomposite structures, we have developed a model for the formation of the current images of the metal NCs in a dielectric film by Tunnelling AFM. The NCs were treated as the metal droplets of a spherical shape with the radius R_c . The model is based on the theory of STM (Tersoff & Hamann, 1985), which, in turn, employs the concept of the tunnel matrix element (Bardeen, 1961):

$$M_{pc} = \frac{\hbar^2}{2m_s} \int (\chi_p^* \nabla \chi_c - \chi_c^* \nabla \chi_p) d\mathbf{S}, \quad (4)$$

where χ_p and χ_c are the envelope wavefunctions of the electrons in the probe and in the NC, p and c are the generalized quantum numbers, indexing the electronic states in the probe and in the NC, respectively. Since we treat the probe coating as a bulk material, it seems reasonable to select $p = \{k_x, k_y, k_z, s\}$ where the first three elements are the respective components of the electron wavevector in the conduction band of the probe coating material and $s = \pm 1/2$ is the spin.

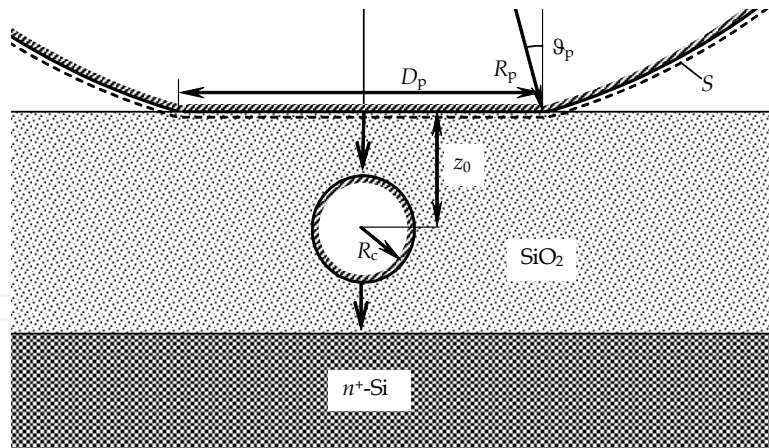


Fig. 10. The schematic of the electron tunneling between a metal coated AFM probe and a metal NC embedded inside a dielectric film on a conductive substrate.

We have considered the electron states both in the probe coating and in the NC to be twofold spin degenerate and therefore have left all the spin-related effects as well as the spin-orbit interaction induced ones beyond the present consideration. In the NC, due to a spherical symmetry of the problem, it seems reasonable to select $c = \{n, l, m, s\}$ where n , l , and m are the radial, orbital, and magnetic quantum numbers, respectively.

According to (Bardeen, 1961), the surface of integration S could be any one located entirely inside the potential barrier between the probe and the NC. We have considered a model probe shape to be a cone with a truncated spherical apex (Fig. 10). We have selected the integration surface S in a close proximity to the model probe surface but at the minimum distance $\delta > k_p^{-1} = \hbar / (2m_0A)^{1/2}$, where A is the workfunction of the probe coating material, and m_0 is the free electron mass. The integration surface S can be divided into the three parts: (i) the area of the contact between the probe and the dielectric film surface that is a circle of the diameter D_p ; (ii) a spherical belt defined by the two polar angles ϑ_p and ϑ_c ; and (iii) a conical side surface of the AFM probe tip. Taking into account a rapid decay of χ_c with increasing distance from the NC surface, one can neglect the contribution of the side cone surface into the integral (4). Following (Tersoff & Haman, 1985), we have selected the probe envelope wavefunction in the range $\vartheta_p < \vartheta < \vartheta_c$ in the asymptotic spherical form valid at least at the distance from the probe surface greater than the decay length of the electron wavefunction in the probe coating δ :

$$\chi_p = C_p \frac{R_p}{|\mathbf{r} - \mathbf{r}_0| \sqrt{\Omega_p}} \exp\left[k_p (R_p - |\mathbf{r} - \mathbf{r}_0|)\right], \quad (5)$$

where Ω_p is the probe volume and $C_p \sim 1$ is the normalizing constant. At $\vartheta < \vartheta_p$ (i. e. within the probe to surface contact area) the probe electron wavefunction was selected in the form:

$$\chi_{pd} = C_d \exp(k_d z). \quad (6)$$

Here $k_d = [2m(A - X_d)]^{1/2} / \hbar$, X_d and m are the electron affinity and the effective electron mass in the dielectric, respectively. The normalizing constant C_d was adjusted to provide the continuity of the probe envelope wavefunction at $\vartheta = \vartheta_p$. Nevertheless, both the magnitude and the direction of the envelope wavefunction gradient still undergo a kink at $\vartheta = \vartheta_p$,

which is a drawback of the model. However, the calculations had shown the contribution of this “edge effect” into the total probe current to be small ($< 0.3\%$) for the selected model parameters (R_p and D_p) so that it could be neglected. Note that at $D_p \rightarrow 0$ the probe envelope wavefunction is reduced to (5) (just this case has been considered by Tersoff & Hamann, 1985). Also, following (Tersoff & Hamann, 1985), we have assumed for simplicity that the workfunctions of the probe coating and NC materials are equal. Also, we have neglected the effect of the kinks of the effective electron mass and of the potential barrier height at the interface between the dielectric film and vacuum on the envelopes and their gradients. The contact area size D_p can be estimated from the solution of Hertz’ problem:

$$D_p = 2\sqrt[3]{\frac{F_n R_p}{K}}, \quad (7)$$

where F_n is the loading force,

$$\frac{1}{K} = \frac{3}{4} \left(\frac{1 - \gamma_p^2}{Y_p} + \frac{1 - \gamma_d^2}{Y_d} \right), \quad (8)$$

$Y_p(Y_d)$ are the Young’s moduli and $\gamma_p(\gamma_d)$ are the Poisson coefficients of the probe coating and the dielectric film materials, respectively. For typical values of $F_n \sim 1$ nN and $R_p \approx 35$ nm, $D_p \sim 10$ nm. The tunneling rate of the electrons from the NC to the substrate Γ_u was assumed to exceed the one from the probe to the NC Γ_c , i. e. the NC was treated as a sink for the electrons with an infinite capacity. Therefore, we neglected the effect of Coulomb blockade considered in the next section.

The envelope wavefunctions of the electron in the NC were selected in the form of the radial part of a well known solution of the Schrödinger’s equation for a spherical quantum dot (QD) with a finite potential barrier height U_0 in the effective mass approximation:

$$\chi_c = \begin{cases} C_i j_l(k_i |\mathbf{r} - \mathbf{r}_c|), & |\mathbf{r} - \mathbf{r}_c| < R_c \\ C_c h_l^{(1)}(ik_c |\mathbf{r} - \mathbf{r}_c|), & |\mathbf{r} - \mathbf{r}_c| > R_c \end{cases} \quad (9)$$

where $j_l(r)$ and $h_l^{(1)}(r)$ are the spherical Bessel and Hankel functions, respectively, $k_i = (2m_c E_F)^{1/2}/\hbar$, $k_c = [2m_d(A - X_d)]^{1/2}/\hbar$, where E_F is the Fermi energy in the NC (probe coating) material, $\mathbf{r}_c = \{0, 0, -z_0\}$ is the position of the NC’s center beneath the dielectric film surface, C_i and C_c are the normalizing constants. We have neglected the angular dependence of χ_c because of the spherical symmetry of the NC and have normalized χ_c to unity as usual:

$$4\pi \int_0^\infty \chi_c(r) r^2 dr = 1. \quad (10)$$

The total probe current is given by (Tersoff & Hamann, 1985)

$$I_t = \frac{2\pi e}{\hbar} \sum_{c,p} |M_{cp}|^2 f(E_p) [1 - f(E_c + eV_g)] \delta(E_c - E_p). \quad (11)$$

In the limit of low voltages ($eV_g \ll A$) and low temperatures $T \ll eV_g/k_B$ where k_B is the Boltzmann constant, (11) can be expanded in the form:

$$I_t = \frac{2\pi e^2 V_g}{\hbar} \sum_c |M_{cp}|^2 \rho_p(E_F), \quad (12)$$

where $\rho_p(E_F)$ is the density of states (DOS) at the Fermi level in the probe coating material. The generalized index c counts the quantum confined states in the NC the energies of which E_c fall in the limits $E_F - eV_g < E_c < E_F$.

In Fig. 11 the model current images of a metal NC with $R_c = 1$ nm calculated for various values of D_p and of the depth of the NC's center position beneath the dielectric film surface z_0 (see Fig. 10) are presented. The two main conclusions important for the interpreting of the Tunnelling AFM results could be made from the modeling.

First, the size of the current image of an individual NC inside a dielectric film was found to be determined by the size of the contact area between the AFM probe tip to the sample surface D_p (Figs. 11 & 12). This is a particular manifestation of the convolution effect (Bukharaev et al., 1997). This effect, in turn, originates from a general principle of the theory of measurements. It claims that the result of any measurement is a convolution of the object function with the measuring instrument one. In STM, $|\chi_c(\mathbf{r})|^2$ and $|\chi_p(\mathbf{r})|^2$ play the roles of the object and measuring functions, respectively. However, in Tunnelling AFM the convolution effect manifests itself in a special way. In ordinary STM (in the constant current mode), the finite R_p results in smoothing and spreading of the features in the STM images: the less R_p , the sharper the STM image. In the limit of a point probe [$\chi_p(\mathbf{r}) \sim \delta(\mathbf{r}_0)$], the STM

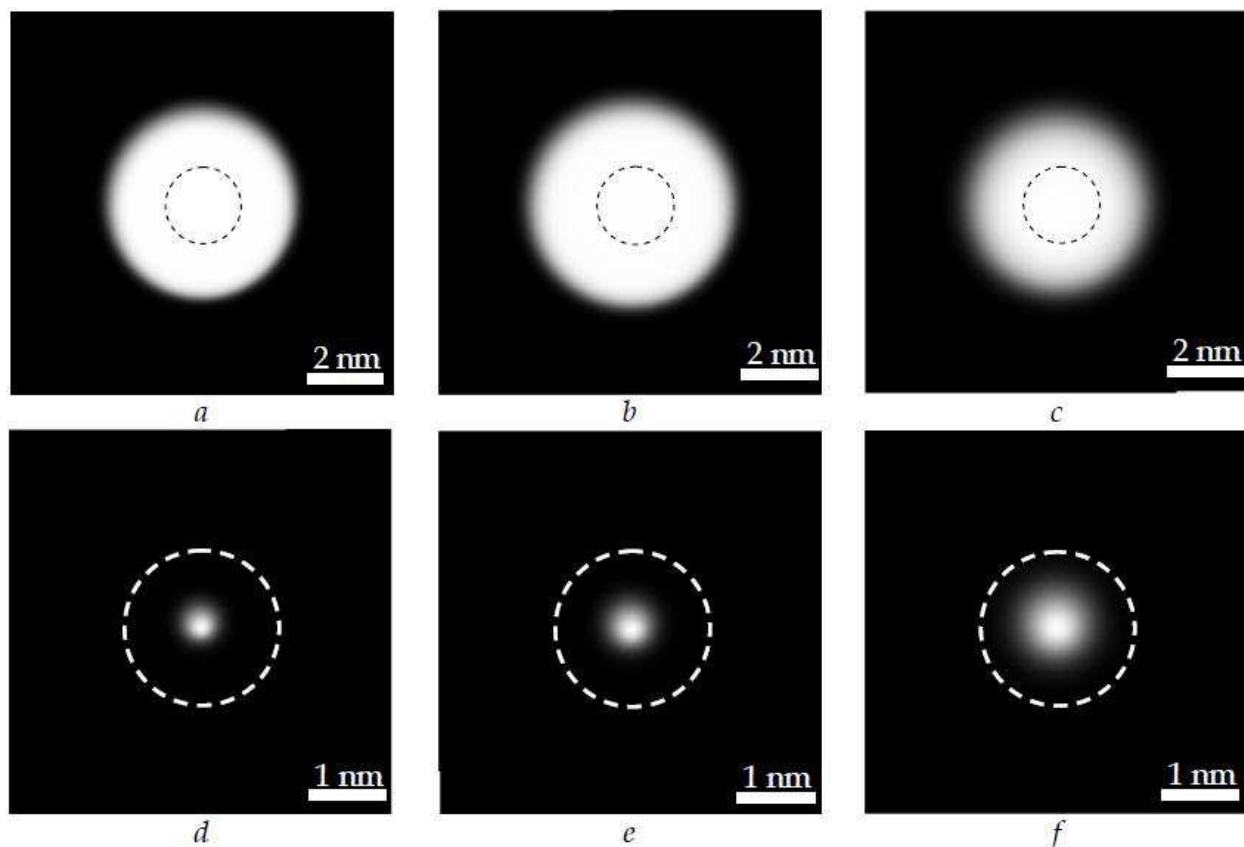


Fig. 11. The model current images $I_t(x, y)$ of a spherical Au NC in a SiO_2 film. $R_c = 1$ nm. R_p , nm: $a - c - 35$, $d - f - 0.1$. D_p , nm: $a - c - 10$, $d - f - 0$. z_0 , nm: $a, d - 1.2$, $b, e - 2.0$, $c, f - 5.0$. The NC's contour is shown by the dashed circle.

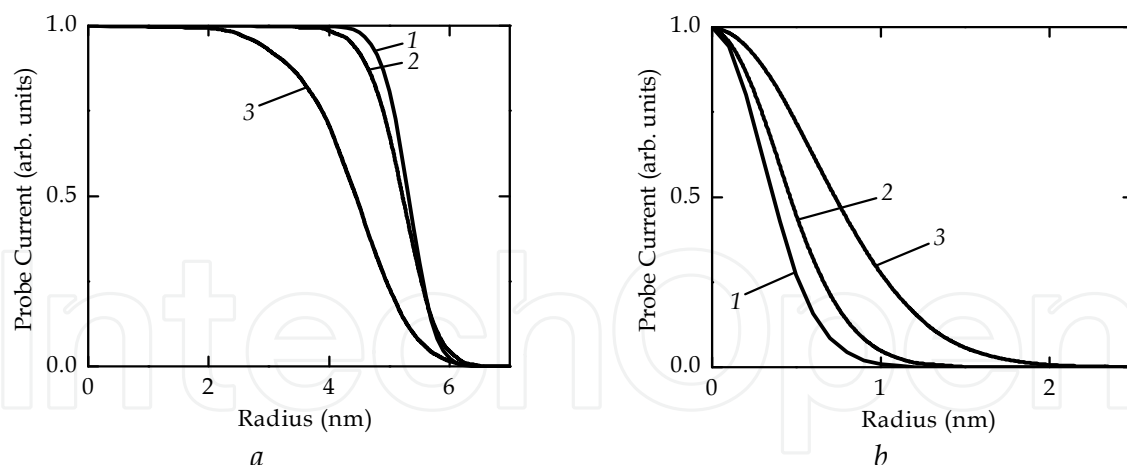


Fig. 12. The normalized model radial current image profiles $I_t(r)$ of a spherical Au NC in a SiO₂ film. $R_c = 1$ nm. R_p , nm: $a - 35$, $b - 0.1$. D_p , nm: $a - 10$, $b - 0$. z_0 , nm: 1 – 1.2, 2 – 2.0, 3 – 5.0.

image reproduces the spatial distribution of the local density of states (LDOS) over the sample surface (Tersoff & Hamann, 1985). In contrary, in Tunnelling AFM the size of the current image of a NC is still determined by D_p even if $R_p \ll R_c$ (Fig. 11, $d-f$ & Fig. 12, a). The latter case takes place in the STM investigation of the granular nanocomposite films (Bar-Sadeh et al., 1994; Imamura et al., 2000). The above effect originates from the fact that the AFM (or STM) probe follows the dielectric film surface in its moving (ideally, at constant height, as in constant height STM mode) and could be understood qualitatively from a simple geometrical consideration (Fig. 10). Due to the fast decay of $\chi_c(r)$ with increasing r , the major contribution into the total probe current I_t is made by the tunneling via the shortest way between the NC and the film surface (shown by an arrow in Fig. 10). The resulting current image is actually the result of the imaging of the probe by this very narrow (δ -like) current channel regardless to R_c .

The second conclusion is the dependence of the size and the contrast of the current image of a NC on the depth of its location beneath the dielectric film surface z_0 . When $D_p \gg R_c$ the size of the NC's current image decreases with increasing z_0 (Fig. 11 $a-c$ & Fig. 12, a). This effect is explained by increasing the relative contribution from the near-polar segments of the NC surface into the total probe current with increasing z_0 . The observation of the current channels of various sizes and contrast in the current image of a nanocomposite SiO₂/SiO₂:NC-Au/SiO₂/ n^+ -Si film (Fig. 9, b) may be considered as an evidence for the suggestion that some NCs nucleate at the upper interface of the nanocomposite layer while the others – at the lower one, as had been discussed in the previous section. When $R_p \ll R_c$ the size of the NC's current image increases with increasing z_0 (Fig. 11 $d-f$ & Fig. 12, b). In both cases, the less z_0 , the sharper the NC's current image. Earlier we had used a quasi classical approach to analyze the formation of the current images of the metal NCs embedded into a dielectric film on a conductive substrate by Tunneling AFM (Lapshina et al., 2008). For $R_c \ll D_p$ the tunnel current

$$I_t = \int_0^{2\pi} \int_0^{\rho_p} j(\rho, \varphi, V_g) \cos(\alpha) \rho d\rho d\varphi, \quad (13)$$

where $j(\rho, \varphi, V_g)$ is the tunnel current density through the element of the probe-to-sample contact area $\rho d\rho d\varphi$. In the quasi classical limit, α takes a meaning of the angle of incidence of the tunneling electrons onto the contact area. In (4) this factor is accounted for by the product $\nabla\chi \cdot d\mathbf{S}$. For $R_c \gg R_p$

$$I_t = R_c^2 \int_0^{2\pi} \int_0^{\vartheta_m} j(\vartheta, \varphi, V_g) \cos(\alpha) \sin \vartheta d\vartheta d\varphi, \quad (14)$$

where ϑ_m is defined by the condition $\cos(\alpha) = 0$. The tunnel current density j was calculated according to Simmons' formula (Simmons, 1963). The results of the model current images calculations using the quasi classical approach agree with the ones obtained using the model described above.

The main advantage of the latter is more accurate accounting for the edge effects. On the other hand, its main drawback is the utilization of the low voltage approximation.

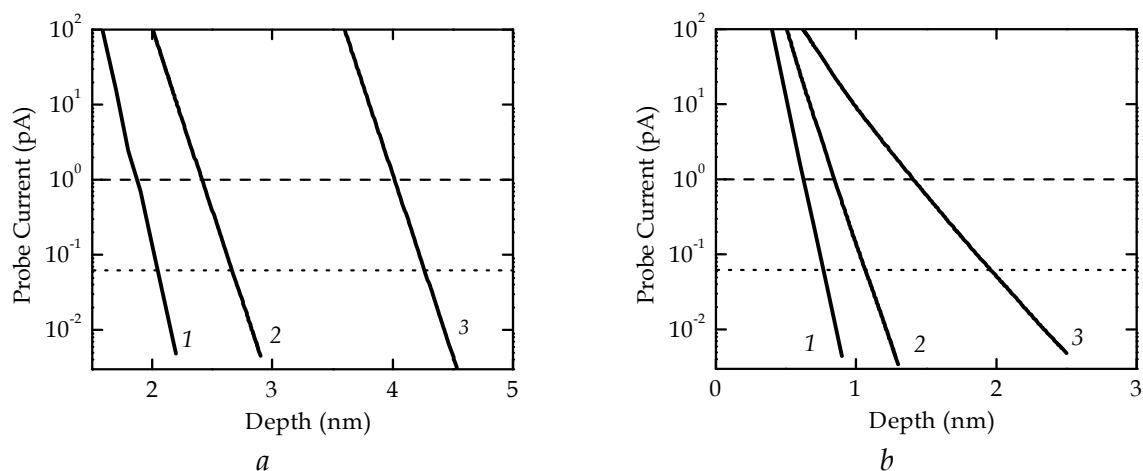


Fig. 13. The model dependences of the probe current I_t on the depth of the Au NC beneath the SiO_2 film surface z_0 calculated in the quasi classical approximation. $R_c = 1$ nm. R_p , nm: $a - 35, b - 0.1$. D_p , nm: $a - 10, b - 0$. V_g , V: 1 - 2, 2 - 6, 3 - 9. The dashed and dotted lines denote the typical noise levels of an ordinary STM preamplifier and for the low-current one, respectively.

Experimentally, a considerable tunnel current I_t (greater than the noise level of the STM preamplifier used ~ 1 pA) has been observed in the strong field regime ($eV_g \sim A$) when the electron tunneling between the probe and the NC goes through the triangle potential barrier (the Fowler-Nordheim mechanism). The expressions for the envelope wavefunctions (5, 6, and 9) are obviously not valid in this case. Using Simmons' formula allowed the evaluation of I_t in both regimes. In particular, it allowed the estimation of the maximal thickness of the dielectric layers in the structures destined to the Tunneling AFM or the STM investigations (Fig. 13, a & b , respectively).

4. Coulomb blockade of the electron tunnelling through individual Au nanoclusters in the SiO_2/Si films

The $I - V$ curves of the probe-to-sample contact measured in the current channels of larger sizes ($D = 5$ to 10 nm) exhibited the Coulomb staircase, more or less expressed (Fig 13, a).

The Coulomb staircase is more pronounced in the differential tunnel spectra of the probe-to-sample contact dI_t/dV_g vs V_g (Fig. 13, *b*) obtained from the measured $I-V$ curves by the numerical differentiation with nonlinear smoothing.

In order to relate the Coulomb staircase period ΔV to the NCs' morphology and to the geometrical parameters of the nanocomposite structures, we have used a model of an ellipsoidal NC (taking into account the flattened shape of the NCs discussed above in Sec. 2) between two flat electrodes (Fig. 14, *a*). The capacitance of a flattened ellipsoidal droplet with respect to a semi-infinite flat metal electrode can be calculated as

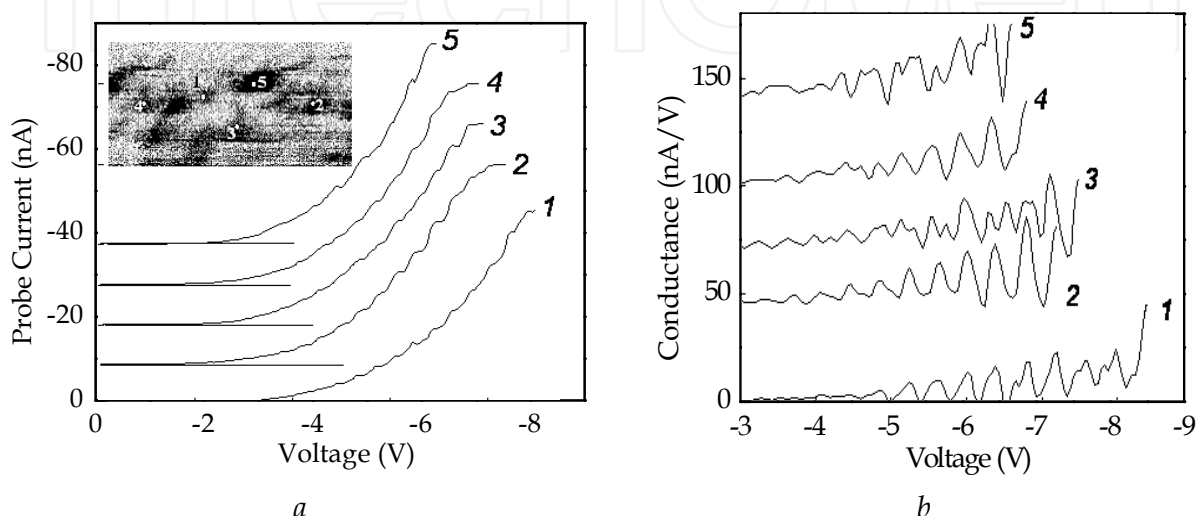


Fig. 13. The $I-V$ curves (*a*) and the respective differential tunnel spectra dI_t/dV_g vs V_g (*b*) of the Pt coated Si AFM probe contact to the SiO₂/ SiO₂:NC-Au/SiO₂/*n*⁺-Si structure measured in different current channels. Reprinted from (Filatov et al., 2010) under license by IoP Publishing Ltd.

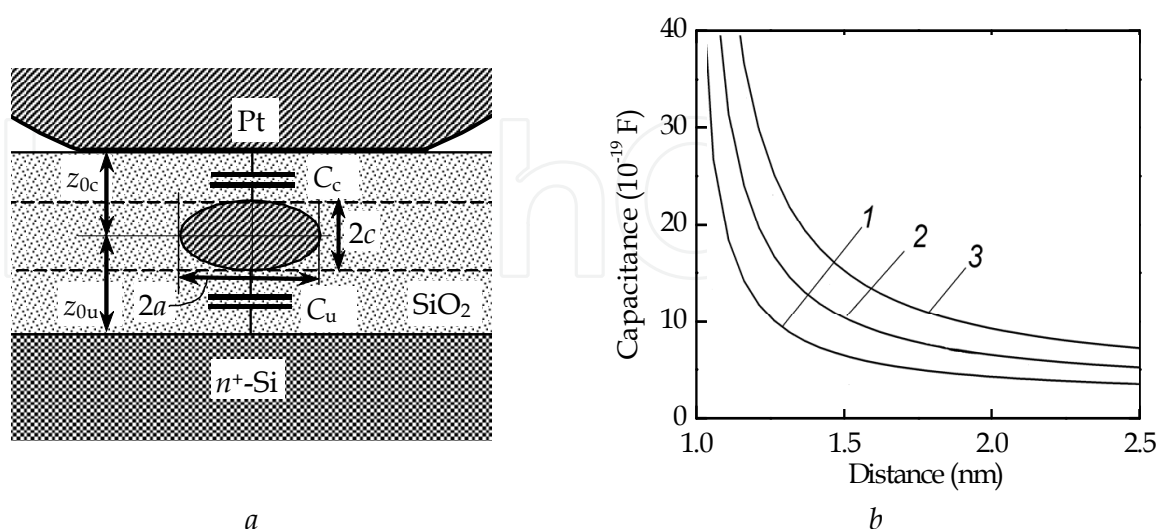


Fig. 14. The calculated dependencies of the capacitance of an ellipsoidal metal NC with respect to a flat metal electrode (*a*) on the separation between the NC centre and the electrode z_0 (*b*). $c = 1$ nm. $a = b$, nm: 1 – 1.5; 2 – 2.0; 3 – 2.5.

$$C^{-1} = \frac{1}{2\pi\epsilon\epsilon_0\sqrt{a^2 - c^2}} \left[\operatorname{arctg}\left(\frac{2z_0 - c}{\sqrt{a^2 - c^2}}\right) - \operatorname{arctg}\left(\frac{c}{\sqrt{a^2 - c^2}}\right) \right], \quad (15)$$

where a and c are the bigger and smaller axes of the ellipsoid (Fig. 14, *a*), ϵ and ϵ_0 are the dielectric constants of the dielectric and vacuum, respectively. The expression (15) can be derived out easily from the well-known one for the capacitance of a lonely flattened metal ellipsoid:

$$C^{-1} = \frac{1}{8\pi\epsilon\epsilon_0\sqrt{a^2 - c^2}} \operatorname{arctg}\left[\frac{\sqrt{a^2 - c^2}}{c}\right], \quad (16)$$

using the image potential method. It should be stressed here that (15) gives only an approximate value of C when $z_0 \sim c$. When deriving out (15) the ellipsoidal NC surface was assumed to be an equipotential one. Obviously, this is not the case when $z_0 \sim c$ because of the polarization of the metal NC induced by the flat electrode. On the other hand, (15) gives the right asymptotic of $C(z_0)$ at $z_0 \rightarrow c$: $C \rightarrow \infty$ (Fig. 14, *b*) while (16) gives a finite value of C that is not true at $z_0 \rightarrow c$ since in this case the NC and the metal electrode contact each other.

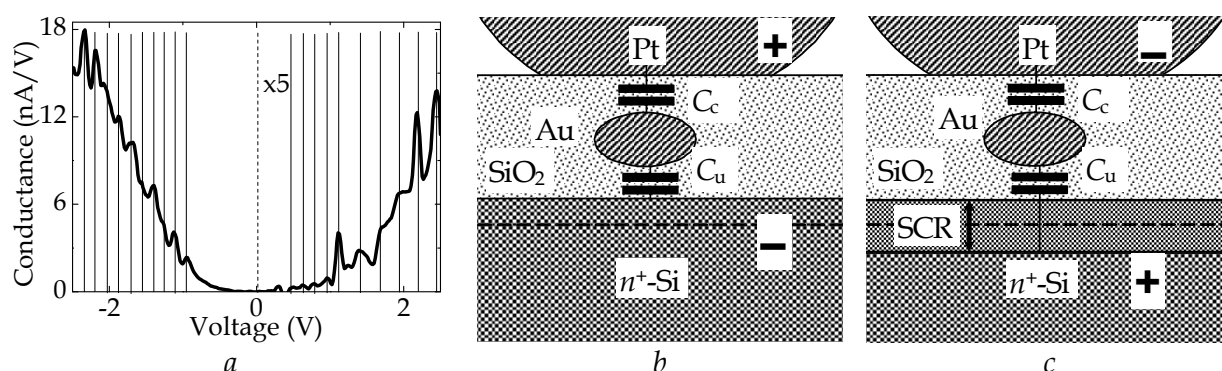


Fig. 15. A differential tunnel spectrum dI_t/dV_g vs V_g of a SiO₂(1.5 nm)/SiO₂:NC-Au(1 nm)/SiO₂(1.5 nm)/n⁺-Si nanocomposite structure (*a*); The effect of the V_g polarity on the capacitance between the Au NC, the probe, and the substrate: *b* – $V_g < 0$; *c* – $V_g > 0$.

For the asymmetric scheme of Coulomb blockade, the period of the Coulomb staircase $\Delta V = e/C_\Sigma$, where $C_\Sigma = C_c + C_u$ (Fig. 14, *a*), C_c and C_u are the capacitances of the metal NC with respect to the probe and to the substrate, respectively (Averin et al, 1991). Assuming $c = 1$ nm, from $\Delta V = 0.4$ to 0.25 V one has $D = 2a = 1.6$ to 2.6 nm which satisfactory agrees with the TEM data.

In some cases, ΔV was different at the different polarities of V_g (Fig. 15, *a*). The effect was attributed to the modulation of the space charge region (SCR) at the SiO₂/n⁺-Si interface by the probe potential (Fig. 15, *b* & *c*). At $V_g > 0$ (Fig. 15, *b*) the SCR thickness decreases, $C_u \gg C_c$, and $C_\Sigma \approx C_u$. At $V_g < 0$ (Fig. 15, *c*) the SCR thickness increases, $C_u \ll C_c$, and $C_\Sigma \approx C_c$.

5. Resonant electron tunnelling through the individual Au nanoclusters in the SiO₂/Si films

The $I-V$ curves measured in the current channels of smaller sizes (3 to 5 nm) are shown in Fig. 16, *a*. The peaks attributed to the resonant tunnelling through the Au NCs are seen at

the negative V_g . The interpretation of the tunnelling spectra was based on a double barrier Pt/SiO₂/Au/SiO₂/Si structure model (Lapshina et al., 2009). The model was based on the exact solution of one-dimensional Schrödinger's equation in the effective mass approximation. The applicability of the one-dimensional model was justified by the flattened shape of the NCs so that they could be treated as thin disks which, in turn, allowed neglecting the size quantization in the film plane. The band diagrams of the model structures were calculated taking into account the band bending at the n^+ -Si/SiO₂ interface. The profile of the potential $\varphi(z)$ in the SCR was calculated from the solution of the one-dimensional Poisson's equation for a uniformly doped semiconductor with the boundary condition at the Si/SiO₂ interface: $\varepsilon_{\text{Si}}F_{\text{Si}} = \varepsilon F$ where ε_{Si} and ε are the dielectric constants of Si and SiO₂, F_{Si} and F are the electric field strengths in Si and SiO₂, respectively:

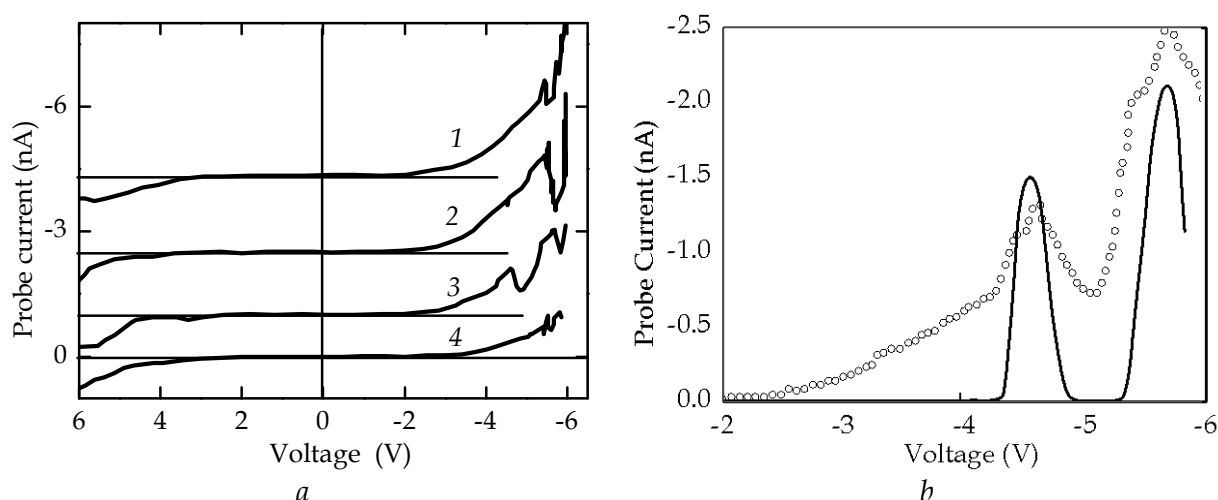


Fig. 16. The $I-V$ curves of the contact of a Pt coated Si AFM probe to the SiO₂(1.5 nm)/SiO₂:NC-Au/SiO₂(1.8 nm)/ n^+ -Si nanocomposite structure measured in different current channels (a); an example of the approximation of a part of curve 3 (circles) by a calculated one (solid line) (b). Reprinted from (Filatov et al., 2010) under license by IoP Publishing Ltd.

$$\varphi(z) = \frac{\varepsilon F}{2\varepsilon_{\text{Si}}l_0} (z - l_0 - z_d)^2. \quad (17)$$

Here l_0 is the SCR thickness and z_d is the position of the SiO₂/Si interface. The NCs were assumed to be depleted completely due to the quantum size effect that allowed neglecting the screening of the electric field F by the electrons confined in the NC. Earlier, the STM/STS and AES studies revealed that the similar Au NCs on the highly oriented pyrolytic graphite (HOPG) surface could undergo the metal-to-insulator transition at $h < 1$ nm (Borman et al., 2006); an energy gap was observed in their tunnel spectra. In this case, the electron-electron scattering inside the NCs would not affect the coherent tunnelling through them. It is not the case for the NCs of larger size ($h > \approx 1$ nm), which are likely filled with the electrons. The part of V_g , which drops on the SCR

$$\Delta\varphi = \frac{\varepsilon F l_0}{2\varepsilon_{\text{Si}}} = \frac{\varepsilon_0 \varepsilon^2 F^2}{2e\varepsilon_{\text{Si}}N_D}, \quad (18)$$

where N_D is the donor concentration in Si. At $V_g \approx 5$ V, $\Delta\phi \approx V_g/2$ (Fig. 17, *a*).

The solution of the Schrödinger's equation in the SiO₂ and Au layers for the potential shown in Fig. 17, *a* can be written as:

$$\chi(z) = C_1 \text{Ai}[s(z)] + C_2 \text{Bi}[s(z)], \quad (19)$$

where Ai and Bi are the Airy functions of the I and II types, respectively, C_1 and C_2 are the normalization constants,

$$s(z) = \frac{(2m)^{1/3}}{(e\hbar F)^{2/3}} [eF(z - z_d) + E_c(z_d) - E], \quad (20)$$

E is the electron energy and $E_c(z_d)$ is the bottom of the conduction band of Au (SiO₂) at the respective position. With respect to SiO₂, taking into account the amorphous state of the material, one should rather consider the mobility gap edge than the conduction band bottom. The origin of the electron energy E was selected at the bottom of the conduction band in the probe coating material (Pt). This solution is valid for any F , including $F > A/ed_c$, i. e. in the strong electric field (or in the Fowler-Nordheim tunnelling mode) and for any E , including $E > A$, i. e. at the tunnelling over the potential barrier.

Let us consider the case of electrons injection from the AFM probe into the Si substrate (i. e. at $V_g < 0$). In this case, the eigenfunctions of the electron states in the Pt and Si layers can be written as usual:

$$\begin{aligned} \chi_e(z) &= \exp(ik_e z) + C_0 \exp(-ik_e z), \\ \chi_c(z) &= C_c \exp(ik_c z), \end{aligned} \quad (21)$$

respectively, where $k_e = (2m_{\text{Pt}}E)^{1/2}/\hbar$ and $k_c = [2m_{\text{Si}}(E - E_{c\text{Si}})]^{1/2}/\hbar$ are the electron wave vectors of the electron eigenstates in Pt and in Si, respectively. For given selection of the normalization constants C , the tunnel transmission coefficient of the double barrier structure

$$T(E) = \frac{m_{\text{Pt}}k_c(E)}{m_{\text{Si}}k_e(E)} |C_c(E)|^2, \quad (22)$$

as follows from the condition of the probability density flux continuity straightforward. Here m_{Pt} and m_{Si} are the electron effective masses in Pt and in Si, respectively. The values of the normalization constants C at given E were found from the Bastard's boundary conditions (the continuity of $\chi(z)$ and of $m^{-1}d\chi/dz$) at each interface in the structure. In Fig. 17, *b* a model tunnel transparency spectrum of the double barrier structure $T(E)$ calculated for $V_g = 5.7$ V is presented.

The total probe current at $V_g < 0$ is given by (Esaki & Stiles, 1966):

$$I_t(V_g) = \frac{em_{\text{Pt}}k_B T D^2}{8\pi\hbar^3} \int_0^\infty T(E, V_g) \ln \left[\exp\left(\frac{E_F - E}{k_B T}\right) + 1 \right] dE. \quad (23)$$

The reverse current was neglected since I_t becomes considerable ($I_t > 1$ pA) at $V_g \geq 2$ V $\gg k_B T/e$ only.

An example of the fitting of a measured $I - V$ curve of the probe-to-sample contact by a model one is presented in Fig. 16, *b*; d_w , d_c , and h were the fitting parameters. The best fit has

been achieved at $d_u = 1.4$ nm, $d_c = 1.1$ nm, and $h = 1.3$ nm (the band diagram in Fig. 17, *a* has been calculated just for these values) which agrees with the XPS and TEM data satisfactory although the model described above is rather rough. First of all, the effect of the image potential at the Pt/SiO₂ and Si/SiO₂ interfaces on the band profile has been neglected. Then, the electron energy distribution has been calculated in the simple parabolic band approximation, the global band minima were taken into account only while the higher band extrema as well as the band nonparabolicity were neglected. Also, the values of the band offset at the SiO₂/Au and SiO₂/Pt interfaces were calculated from the values of the workfunction and of the electron affinity for the respective materials.

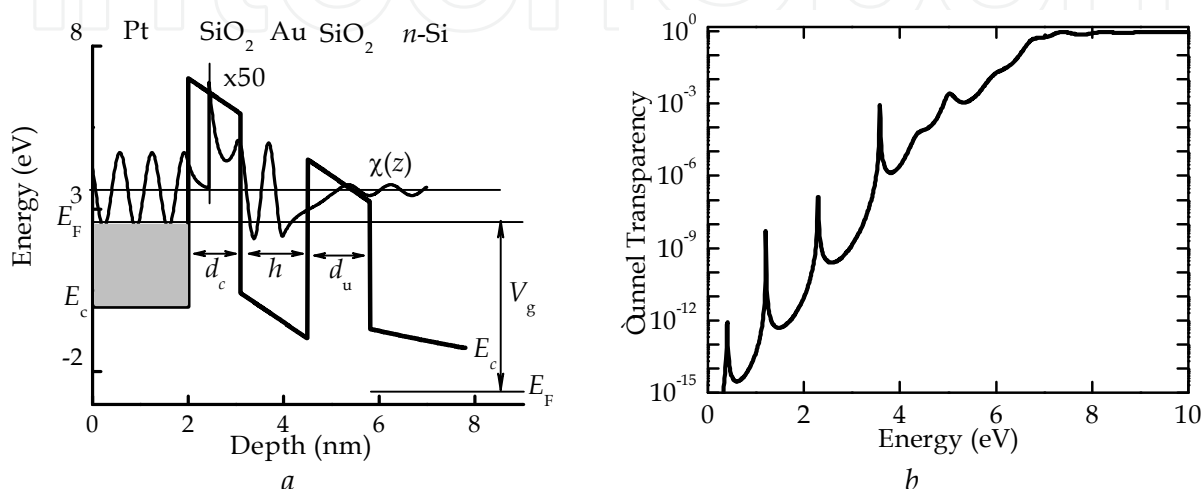


Fig. 17. The calculated band diagram (*a*) and the tunnel transparency spectrum (*b*) for a Pt/SiO₂/Au/SiO₂/*n*⁺-Si double barrier structure. $d_c = 1.1$ nm, $h = 1.3$ nm, $d_u = 1.4$ nm, $V_g = 5.7$ V. Reprinted from (Filatov et al., 2010) under license by IoP Publishing Ltd.

In addition, the dielectric constant ϵ for such an exotic material as depleted Au layer was not known, so it was assumed to be equal to the one of SiO₂ to simplify the model. Nevertheless, from the comparison of the results of the modeling with the experimental data (Fig. 16, *b*) one can conclude that the present model describes the electron tunnelling through the small Au NCs in a thin SiO₂ film satisfactory and that it is likely the peaks observed in the measured $I - V$ curves originate from the resonant tunnelling effect.

In Fig. 16, *b* one can notice that the resonant peaks in the calculated $I - V$ curve are narrower compared to the measured ones that should be attributed to the inhomogeneous broadening due to the nonuniformity of the actual NC thickness. Also, one can note the splitting of the resonant peaks in the measured $I - V$ curve that could probably be ascribed to the stepwise fluctuations in the NC thickness.

6. Conclusion

The results presented in this chapter demonstrate the approaches based on the deposition of a nm-thick Me-Si (Me = Au, Pt) amorphous mixture with well-controlled Me/Si compositional ratio followed by its oxidation by the glow discharge oxygen plasma at room temperature or alternatively by its thermal oxidation to allow growing the ultrathin SiO₂ layers with the embedded Me NCs. The resulting SiO₂:NC-Me nanocomposite layers contain the Me NCs of 2 to 5 nm in the lateral size with the sheet density of $\sim 10^{13}$ cm⁻², which can be

controlled by varying the Me/Si ratio in the initial Me–Si mixture. Furthermore, the methods allow growing the $\text{SiO}_2/\text{SiO}_2\text{:NC-Me}/\text{SiO}_2$ sandwiched nanocomposite structures on any substrate in a single vacuum cycle. It should be stressed here that the NCs formed by the proposed methods are confined in the single sheets with the precisely controlled thickness of the underlying and cap layers. The $C - V$ measurements demonstrated a clearly expressed hysteresis indicating that the nanocomposite MOS structures grown by the described methods have the potential for the nanoscale nonvolatile memory applications.

The application of the Tunneling AFM allowed the visualization of the Au NCs embedded into the ultrathin SiO_2 films on the Si substrates. The size of the current image of a NC embedded in a thin dielectric film was found to be determined primarily by the size of the contact area between the AFM probe and the film surface. The second factor affecting the image size and contrast was found to be the depth of the NC's location beneath the film surface. The application of Tunneling AFM allowed also the observation of the Coulomb blockade and of the resonant electron tunnelling through the individual Au NCs ~ 1 nm in thickness. The observed effects can be utilized in future nanoelectronic devices based on single NCs embedded in ultrathin dielectric films.

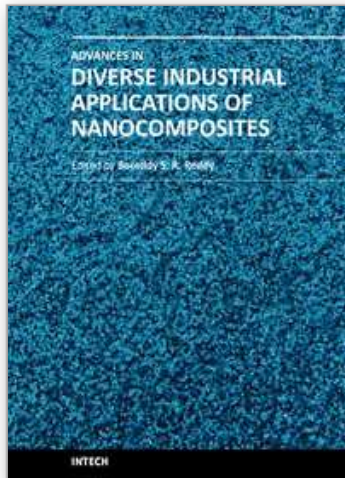
7. References

- Antonov, D.A.; Gorshkov, O.N.; Kasatkin, A.P.; Maximov, G.A.; Saveliev, D.A.; & Filatov, D.O. (2004). Investigation of the electronic properties of the Zr nanoclusters in the YSZ films by Combined STM/AFM. *Physics of Low - Dimensional Structures*, 1/2 (January 2004), 139-142, 0204-3467.
- Antonov, D.A.; Filatov, D.O.; Zenkevich, A.V. & Lebedinskii Yu.Yu. (2007). Investigation of the electronic properties of Au nanoclusters in SiO_2 by Combined Scanning Tunneling/Atomic Force Microscopy. *Bulletin RAS: Physics*, 71, 1 (January 2007), 56-58, 1062-8738.
- Averin, D.V.; Korotkov, A.N. & Likharev, K.K. (1991). Theory of single-electron charging of quantum wells and dots. *Phys. Rev. B*, 44, 12 (September 1991), 6199-6211, 1098-0121.
- Bardeen, J. (1961). Tunnelling from a many-particle point of view. *Phys. Rev. Lett.*, 6, 2 (January 1961), 57-59, 0031-9007.
- Bar-Sadeh, E.; Goldstein, Y.; Zhang, C.; Deng, H.; Abeles, B. & Millo, O. (1994). Single-electron tunneling effects in granular metal films. *Phys. Rev. B*, 50, 12 (September 1994), 8961-8964, 1098-0121.
- Bonafos, C.; Garrido, B.; Lopez, M.; Perez-Rodriguez, A.; Morante, J.R.; Kihn, Y.; Ben Assayag, G. & Claverie, A. (2000). An electron microscopy study of the growth of Ge nanoparticles in SiO_2 . *Appl. Phys. Lett.*, 76, 26 (June 2000), 3962-8964, 0003-6951.
- Borman, V.D.; Borisyuk, P.V.; Lebid'ko, V.V.; Pushkin, M.A.; Tronin, V.N.; Troyan, V.I.; Antonov, D.A. & Filatov, D.O. (2006). A study of many-body phenomena in metal nanoclusters (Au, Cu) close to their transition to the nonmetallic state. *JETP*, 102, 2 (February 2006), 303-313, 1063-7761.
- Bukharaev, A.A.; Berdunov, N.V.; Ovchinnikov, D.V. & Salikhov, K.M. (1998). Three-dimensional probe and surface reconstruction for Atomic Force Microscopy using a deconvolution algorithm. *Scanning Micros.*, 12, 1 (January 1998), 225-234, 0891-7035.
- Cho, S.H.; Lee, S.; Ku, D.Y.; Lee, T.S.; Cheong, B.; Kim, W.M. & Lee, K.S. (2004). Growth behavior and optical properties of metal-nanoparticle dispersed dielectric thin films

- formed by alternating sputtering. *Thin Solid Films*, 447-448, 1 (January 2004), 68-73, 0040-6090.
- Esaki, L. & Stiles, P.J. (1966). New type of negative resistance in barrier tunneling. *Phys. Rev. Lett.*, 16, 24 (June 1966), 1108-1110, 0031-9007.
- Filatov, D.O.; Lapshina, M.A.; Antonov, D.A.; Gorshkov, O.N.; Zenkevich, A.V. & Lebedinskii, Yu.Yu. (2010). Resonant tunnelling through individual Au nanoclusters embedded in ultrathin SiO₂ films studied by Tunnelling AFM. *J. Phys. Conf. Ser.*, 245 (September 2010) 012018, 1742-6596.
- Guo, L.; Leobandung, E. & Chou, S.Y. (1997). A silicon single-electron transistor memory operating at room temperature. *Science*, 275, 5300 (January 1997) 649-651, 0036-8075.
- Hiraki, A.; Lugujo, E. & Mayer, J.W. (1972). Formation of silicon oxide over gold layers on silicon substrates. *J. Appl. Phys.*, 43, 9 (September 1972), 3643-3650, 0021-8979.
- Hochella Jr., M.F. & Carim, A.H. (1988). A reassessment of electron escape depths in silicon and thermally grown silicon dioxide thin films. *Surf. Sci. Lett.*, 197, 3 (March 1988), L260-L268, 0039-6028.
- Imamura, H.; Chiba, J.; Mitani, S. & Takanashi, K. (2000). Coulomb staircase in STM current through granular films. *Phys. Rev. B*, 61, 1 (January 2000), 46-49, 1098-0121.
- Lapshina, M.A.; Filatov, D.O. & Antonov, D.A. (2008). Current imaging in Combined STM/AFM of metal nanoclusters in dielectric films. *J. Surf. Investigation: X-ray, Synchrotron & Neutron Techn.*, 2, 4 (April 2008), 616-619, 1027-4510.
- Lapshina, M.A.; Filatov, D.O.; Antonov, D.A. & Barantsev, N.S. (2009). Study of resonant tunneling in Au nanoclusters on the surface of SiO₂/Si thin films using the Combined Scanning Tunneling Microscopy and Atomic-Force Microscopy technique. *J. Surf. Investigation: X-ray, Synchrotron & Neutron Techn.*, 3, 4 (April 2009), 559-565, 1027-4510.
- Lebedinskii, Yu.Yu.; Zenkevich, A.; Gusev, E.P. & Gribelyuk, M. (2005). *In situ* investigation of growth and thermal stability of ultrathin Si layers on the HfO₂/Si(100) high- κ dielectric system. *Appl. Phys. Lett.*, 86, 19 (May 2005), 1904-1906, 0003-6951.
- Maksimova, K.Yu.; Matveev, Yu.A.; Zenkevich, A.V.; Nevolin, V.N.; Novikov, A.G.; Gaiduk, P.I. & Orekhov, A.C. (2010). Investigation of the SiO₂:Me nanocomposite structures formed by the metal segregation at the front of silicon oxidation in the Si:Me layers. *Perspektivnye Materialy (Promising Materials)*, 2010, 2 (April 2010), 33-38 (in Russian), 2075-1133.
- Ren, F.; Heng, X.; Guang, X.; Cai, X.; Wang, J.B. & Jiang, C.Z. (2009). Engineering embedded metal nanoparticles with ion beam technology. *Appl. Phys. A*, 96, 2 (August 2009), 317-325, 0947-8396.
- Ruffino, F.; de Bastiani, R.; Grimaldi, M.G.; Bongiorno, C.; Giannazzo, F.; Roccaforte, F.; Spinella, C. & Raineri, V. (2007). Self-organization of Au nanoclusters on the SiO₂ surface induced by 200 keV-Ar⁺ irradiation. *Nucl. Instr. Meth. B*, 257, 1-2, (April 2007), 810-814, 0168-583X.
- Ruffino, F. & Grimaldi, M.G. (2007). Structural and electrical characterization of gold nanoclusters in thin SiO₂ films: Realization of a nanoscale tunnel rectifier. *Microelectron. Eng.*, 84, 3 (March 2007), 532-537, 0167-9317.

- Simmons, J.G. (1963). Generalized formula for the electric tunnel effect between similar electrodes separated by a thin insulating film. *J. Appl. Phys.*, 34, 6 (June 1963), 1793-1804, 0021-8979.
- Tersoff, J. & Hamann, D.B. (1985). Theory of the scanning tunneling microscope. *Phys. Rev. B*, 31, 2 (January 1985), 805-813, 1098-0121.
- Tiwari, S.; Rana, F.; Hanafi, H.; Hartstein, A.; Crabbe, E. F. & Chan, K. (1996). A silicon nanocrystals based memory. *Appl. Phys. Lett.*, 68, 10 (March 1996) 1377-1379, 0003-6951.
- Tiwari, S.; Wahl, J.A.; Silva, H.; Rana, F. & Welser, J.J. (2000). Small silicon memories: confinement, single-electron, and interface state considerations. *Appl. Phys. A*, 71, 4 (October 2000), 403-414, 0947-8396.
- Yanev, V.; Rommel, M.; Lemberger, M.; Petersen, S.; Amon, B.; Erlbacher, T.; Bauer, A.J.; Ryssel, H.; Paskaleva, A.; Weinreich, W.; Fachmann, C.; Heitmann, J. & Schroeder, U. (2008). Tunneling atomic-force microscopy as a highly sensitive mapping tool for the characterization of film morphology in thin high-*k* dielectrics. *Appl. Phys. Lett.* 92, 25 (June 2008), 2910-2912, 0003-6951.
- Yano, K.; Ishii, T. Hashimoto, T.; Kobayashi, T.; Murai, F. & Seki, K. (1994). Room-temperature single-electron memory. *IEEE Trans. Electron Dev.*, 41, 9, (September 1994), 1628-1638, 0018-9383.
- Zacharias, M.; Heitmann, J.; Scholz, R.; Kahler, U.; Schmidt, M. & Bläsing, J. (2002). Size-controlled highly luminescent silicon nanocrystals: a SiO/SiO₂ superlattice approach. *Appl. Phys. Lett.*, 80, 4 (January 2002), 661-664, 0003-6951.
- Zenkevich, A.V.; Lebedinskii, Yu.Yu.; Timofeyev, A.A.; Isayev, I.A. & Tronin, V.N. (2009). Formation of ultrathin nanocomposite SiO₂:nc-Au structures by Pulsed Laser Deposition. *Appl. Surf. Sci.*, 255, 10 (March 2009), 5355-5358, 0169-4332.

IntechOpen



Advances in Diverse Industrial Applications of Nanocomposites

Edited by Dr. Boreddy Reddy

ISBN 978-953-307-202-9

Hard cover, 550 pages

Publisher InTech

Published online 22, March, 2011

Published in print edition March, 2011

Nanocomposites are attractive to researchers both from practical and theoretical point of view because of combination of special properties. Many efforts have been made in the last two decades using novel nanotechnology and nanoscience knowledge in order to get nanomaterials with determined functionality. This book focuses on polymer nanocomposites and their possible divergent applications. There has been enormous interest in the commercialization of nanocomposites for a variety of applications, and a number of these applications can already be found in industry. This book comprehensively deals with the divergent applications of nanocomposites comprising of 22 chapters.

How to reference

In order to correctly reference this scholarly work, feel free to copy and paste the following:

Andrei Zenkevich, Yuri Lebedinskii, Oleg Gorshkov, Dmitri Filatov and Dmitri Antonov (2011). Structural and Electron Transport Properties of Ultrathin SiO₂ Films with Embedded Metal Nanoclusters Grown on Si, *Advances in Diverse Industrial Applications of Nanocomposites*, Dr. Boreddy Reddy (Ed.), ISBN: 978-953-307-202-9, InTech, Available from: <http://www.intechopen.com/books/advances-in-diverse-industrial-applications-of-nanocomposites/structural-and-electron-transport-properties-of-ultrathin-sio2-films-with-embedded-metal-nanocluster>

INTECH
open science | open minds

InTech Europe

University Campus STeP Ri
Slavka Krautzeka 83/A
51000 Rijeka, Croatia
Phone: +385 (51) 770 447
Fax: +385 (51) 686 166
www.intechopen.com

InTech China

Unit 405, Office Block, Hotel Equatorial Shanghai
No.65, Yan An Road (West), Shanghai, 200040, China
中国上海市延安西路65号上海国际贵都大饭店办公楼405单元
Phone: +86-21-62489820
Fax: +86-21-62489821

© 2011 The Author(s). Licensee IntechOpen. This chapter is distributed under the terms of the [Creative Commons Attribution-NonCommercial-ShareAlike-3.0 License](#), which permits use, distribution and reproduction for non-commercial purposes, provided the original is properly cited and derivative works building on this content are distributed under the same license.

IntechOpen

IntechOpen